LETTER

doi:10.1038/nature19059

The active site of low-temperature methane hydroxylation in iron-containing zeolites

Benjamin E. R. Snyder[1]*, Pieter Vanelderen[1,2]*, Max L. Bols[2], Simon D. Hallaert[3], Lars H. Böttger[1], Liviu Ungur[3]†, Kristine Pierloot[3], Robert A. Schoonheydt[2], Bert F. Sels[2] & Edward I. Solomon[1,4]

An efficient catalytic process for converting methane into methanol could have far-reaching economic implications. Iron-containing zeolites (microporous aluminosilicate minerals) are noteworthy in this regard, having an outstanding ability to hydroxylate methane rapidly at room temperature to form methanol[1–3]. Reactivity occurs at an extra-lattice active site called α-Fe(II), which is activated by nitrous oxide to form the reactive intermediate α-O[4,5]; however, despite nearly three decades of research[5], the nature of the active site and the factors determining its exceptional reactivity are unclear. The main difficulty is that the reactive species—α-Fe(II) and α-O—are challenging to probe spectroscopically: data from bulk techniques such as X-ray absorption spectroscopy and magnetic susceptibility are complicated by contributions from inactive 'spectator' iron. Here we show that a site-selective spectroscopic method regularly used in bioinorganic chemistry can overcome this problem. Magnetic circular dichroism reveals α-Fe(II) to be a mononuclear, high-spin, square planar Fe(II) site, while the reactive intermediate, α-O, is a mononuclear, high-spin Fe(IV)=O species, whose exceptional reactivity derives from a constrained coordination geometry enforced by the zeolite lattice. These findings illustrate the value of our approach to exploring active sites in heterogeneous systems. The results also suggest that using matrix constraints to activate metal sites for function—producing what is known in the context of metalloenzymes as an 'entatic' state[6]—might be a useful way to tune the activity of heterogeneous catalysts.

No spectroscopic feature of α-Fe(II) has thus far been discovered[7]. We have now identified Fe(II) ligand-field bands in the diffuse reflectance ultraviolet–visible (DR-UV-vis) spectra of three iron-containing zeolites (Fe-zeolites) that are known to contain α-Fe(II) (see Extended Data Fig. 1)[4,8–10]. Of these, we chose the Fe(II)-beta (BEA) zeolite for further study because of the higher intensity of its ligand-field bands (see Extended Data Fig. 2 for the structure of the BEA lattice). The DR-UV-vis spectrum of Fe(II)-BEA (Fig. 1a) is characterized by an intense band at 40,000 cm^{-1}, and three weak ligand-field bands at 15,900 cm^{-1}, 9,000 cm^{-1} and <5,000 cm^{-1} (a shoulder). To determine which of these bands correlates with α-Fe(II), we activated the sample with nitrous oxide (N_2O; Fig. 1b) and then reacted it with methane (CH_4) at room temperature (Fig. 1c). During activation by N_2O, the 15,900 cm^{-1} band of Fe(II)-BEA is replaced by a new feature of similar intensity at 16,900 cm^{-1}, along with a weak feature at around 5,000 cm^{-1}. The 16,900 cm^{-1} and 5,000 cm^{-1} bands present after N_2O activation disappear upon reaction with CH_4; we therefore assign these bands to α-O. These are the first absorption features to be conclusively attributed to α-O on the basis of their reactivity to CH_4. The 15,900 cm^{-1} band present before N_2O activation is assigned to α-Fe(II). The 5,000–13,000 cm^{-1} region of the CH_4-reacted spectrum overlaps with that of Fe(II)-BEA, indicating that features in this region originate from inactive 'spectator' sites.

The 15,900 cm^{-1} band of α-Fe(II) is an interesting spectral feature, as it is unusual to observe Fe(II) ligand-field bands in this high-energy region. Correlation of Fe(II) sites with hard O/N donors suggests that a band in this region is characteristic of square-planar sites with a spin (S) of 2 (refs 11–15). Importantly, the 15,900 cm^{-1} band is also a spectroscopic handle that enables selective study of α-Fe(II) by variable-temperature variable-field magnetic circular dichroism (VTVH-MCD) spectroscopy.

Low-temperature magnetic circular dichroism (MCD) data from Fe(II)-BEA stabilized in perfluorocarbon glass are shown in Fig. 2a, along with ligand-field DR-UV-vis data for comparison. On the basis of the DR-UV-vis results, the positive MCD feature at 15,100 cm^{-1}

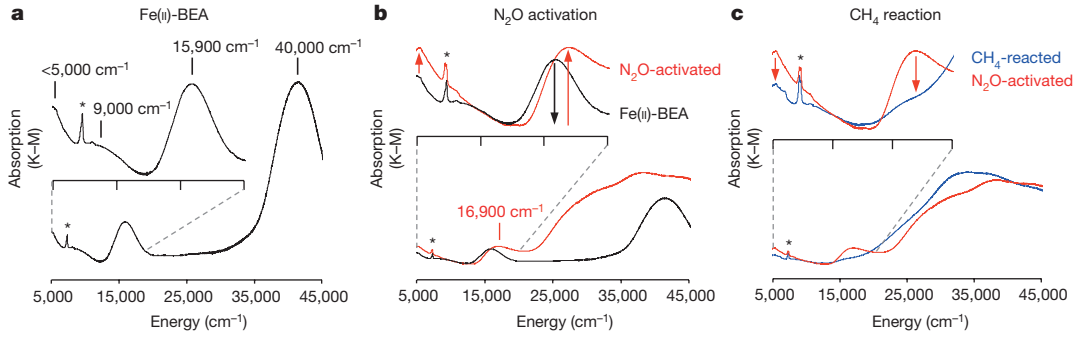

Figure 1 | DR-UV-vis spectra of Fe-BEA in Kubelka–Munk units[31]. **a**, Spectrum for Fe-BEA (Si/Al = 12, 0.3 wt% Fe) after treatment with helium (900 °C, 2 hours) and reduction with hydrogen (700 °C, 1 hour) to produce Fe(II)-BEA. The overall spectrum is shown at the bottom, with an expanded portion of it above. * = OH overtone. **b**, **c**, The spectra resulting from activation of Fe(II)-BEA with N_2O at 250 °C for 15 minutes (**b**), followed by reaction with CH_4 at room temperature (**c**). Key spectral changes are indicated with arrows.

[1]Department of Chemistry, Stanford University, Stanford, California 94305, USA. [2]Department of Microbial and Molecular Systems, Centre for Surface Chemistry and Catalysis, KU Leuven – University of Leuven, Celestijnenlaan 200F, B-3001 Leuven, Belgium. [3]Department of Chemistry, KU Leuven, Celestijnenlaan 200F, B-3001 Leuven, Belgium. [4]Photon Science, SLAC National Accelerator Laboratory, 2575 Sand Hill Road, Menlo Park, California 94025, USA. †Present address: Division of Theoretical Chemistry, Lund University, PO Box 124, 221 00 Lund, Sweden. *These authors contributed equally to this work.

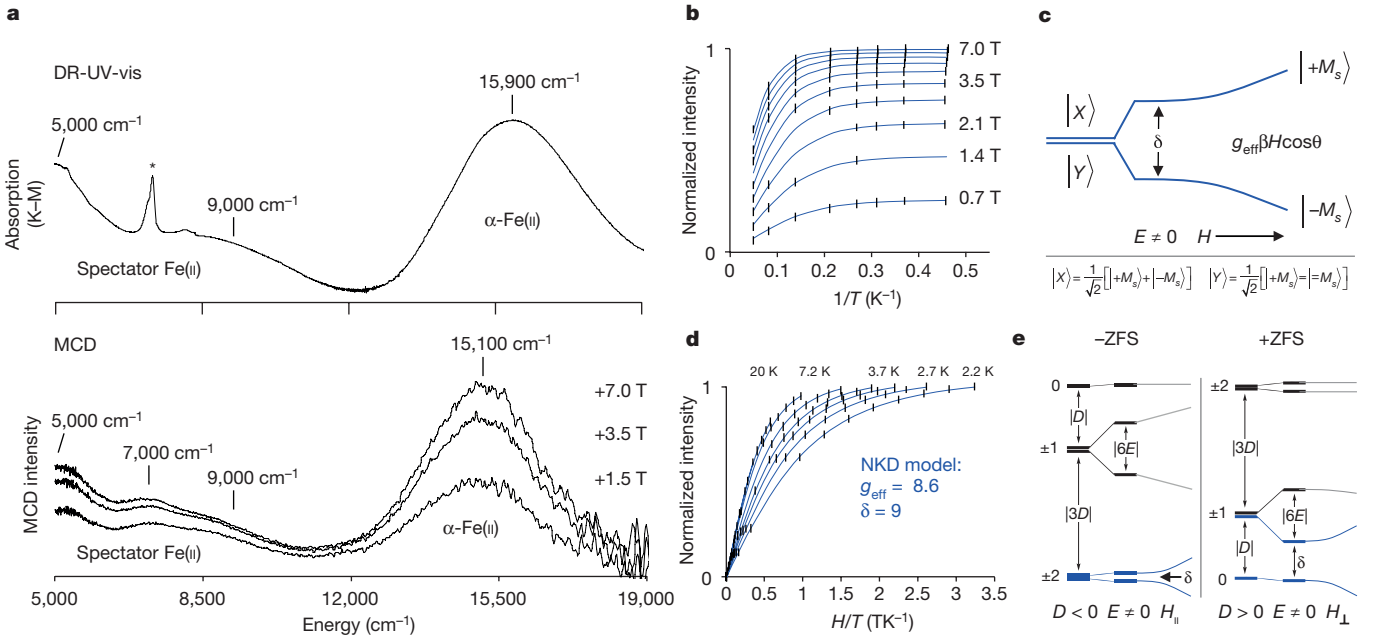

Figure 2 | MCD and VTVH-MCD of α-Fe(II). a, Comparison of the 298 K DR-UV-vis data (reproduced from Fig. 1a; * = OH overtone) and variable-field 3 K MCD data from Fe(II)-BEA (Si/Al = 12, 0.3 wt% Fe). **b**, Saturation magnetization isofields for the 15,100 cm^{-1} band (± 1σ error bars are in black; the fit is in blue). T, tesla; T, temperature. **c**, Influence of rhombic zero-field splitting (ZFS) and magnetic field (parameterized by δ and g_{eff}, respectively) on a non-Kramers doublet (NKD). At zero field, the NKD is split in energy by the rhombic ZFS. The $\pm M_s$ wavefunctions also mix equally, to form $|X\rangle$ and $|Y\rangle$. Application of a magnetic field further splits the levels, and changes the wavefunctions to pure $|-M_s\rangle$ and $|+M_s\rangle$ in high fields. **d**, Saturation magnetization isotherms for α-Fe(II) (fit in blue using the NKD model in **c**). **e**, Comparison of +ZFS and –ZFS $S = 2$ spin manifolds, including effects due to axial ($D \neq 0$) and rhombic ($E \neq 0$) ZFS. Levels identified with the non-Kramers doublet model shown in **c** are highlighted in blue.

is correlated with α-Fe(II), while the weak positive features between 5,000 cm^{-1} and 10,000 cm^{-1} are attributed to spectator sites. The 15,100 cm^{-1} MCD band of α-Fe(II) is sensitive to both field and temperature. This defines α-Fe(II) as paramagnetic at low temperatures. The oxo-bridged[16] and hydroxo-bridged[17] 2Fe(II) structures proposed for α-Fe(II) are therefore excluded, as they would be strongly antiferromagnetically coupled (with an antiferromagnetic coupling constant of more than 10 cm^{-1})[18].

The temperature and field dependence of the 15,100 cm^{-1} MCD feature provides direct insight into the ground state of α-Fe(II)—even in the presence of paramagnetic spectator sites. VTVH-MCD isofields for the 15,100 cm^{-1} band are shown in Fig. 2b. The field dependence of the low-temperature saturation limit reflects variation of the α-Fe(II) ground state with field, indicating that α-Fe(II) is a non-Kramers (integer-spin) system[11,18]. The influence of temperature and field on MCD intensity from a non-Kramers doublet is parameterized by an effective g value (g_{eff}) and a rhombic zero-field splitting (ZFS), δ (Fig. 2c). g_{eff} and δ are related to molecular-spin Hamiltonian parameters, and therefore encode information about site geometry and electronic structure (see Methods for detail). VTVH-MCD isotherms from the 15,100 cm^{-1} band plotted against the ratio of the applied magnetic field and the temperature (H/T) (Fig. 2d) are highly nested (that is, they do not overlap), indicating that δ is large for α-Fe(II)[11,18]. Fitting a non-Kramers-doublet model to VTVH-MCD data enables quantification of δ at 9 cm^{-1} and g_{eff} at 8.6. A g_{eff} close to 8 is consistent with either mononuclear high-spin ($S = 2$) Fe(II), or a high-spin 2Fe(II) dimer with oppositely signed ZFS for each Fe(II)[11,18]. We exclude the latter possibility with Mössbauer data (Extended Data Fig. 3), which show a single quadrupole doublet for α-Fe(II) (isomer shift (IS) = 0.89 mm s^{-1}; quadrupole splitting ($|QS|$) = 0.55 mm s^{-1}; 93% of total Fe). VTVH-MCD therefore defines α-Fe(II) as a mononuclear, square planar Fe(II) site.

Different coordination geometries can be distinguished on the basis of the sign of the axial ZFS parameter, D. A large δ of 9 cm^{-1} is well outside the range possible for a negative ZFS ground state (for which δ is generally smaller than 6 cm^{-1}). D is therefore positive for α-Fe(II) (see Fig. 2e and Methods)[11,18,19]. Fitting a positive ZFS $S = 2$ model to VTVH-MCD data enables quantification of the axial and rhombic ZFS parameters, $D = 13 \pm 1$ cm^{-1} and $E = 1.8 \pm 0.5$ cm^{-1} respectively, as well as a molecular $g_{\perp} = 2.15$ (see Methods for detail). Coupled with electronic structure calculations (*vide infra*), these parameters provide detailed insight into the ligand field of α-Fe(II).

With α-Fe(II) defined as a high-spin monomer, additional information can be extracted from its ligand-field spectrum and spin Hamiltonian parameters. The high energy (>12,000 cm^{-1}) of the 15,900 cm^{-1} DR-UV-vis ligand-field band rules out octahedral, tetrahedral and trigonal bipyramidal geometry for α-Fe(II). Square pyramidal (weak axial) geometry leads to a negative ZFS ground state, and is excluded[11]. Square planar structures, however, are associated with spin Hamiltonian and Mössbauer parameters that are highly similar to those of α-Fe(II)[13–15,20,21]. On this basis, we assign α-Fe(II) as a square planar $S = 2$ Fe(II) site. The ligand-field origins of the spectroscopic features of α-Fe(II) are presented in the Methods.

Within the BEA lattice, only the β-type six-membered ring (β-6MR) motifs shown in Fig. 3a have the appropriate geometry to stabilize a CH_4-accessible square planar site[22]. These three β-6MRs yield highly similar Fe(II)-bound sites (Extended Data Fig. 4); ring A1 is presented here. Data presented in Extended Data Fig. 5 (see Methods for detail) indicate that α-Fe(II) only forms in β-6MRs containing two aluminium T-sites (anionic AlO_4 tetrahedra), and that three configurations of these aluminium T-sites are possible for BEAs that have a silicon/aluminium ratio of more than 10 (a silicon/aluminium ratio of more than 12 was used here)[23,24]. We created density functional theory (DFT) cluster models to evaluate the influence of aluminium configuration on the resulting Fe(II)-bound site (Fig. 3b). The cluster models were geometry optimized on the quintet surface, and are all approximately square planar. T4/T4′ and T8/T8′ bind Fe(II) with two neutral $_{Si}O_{Si}$ ligands and two

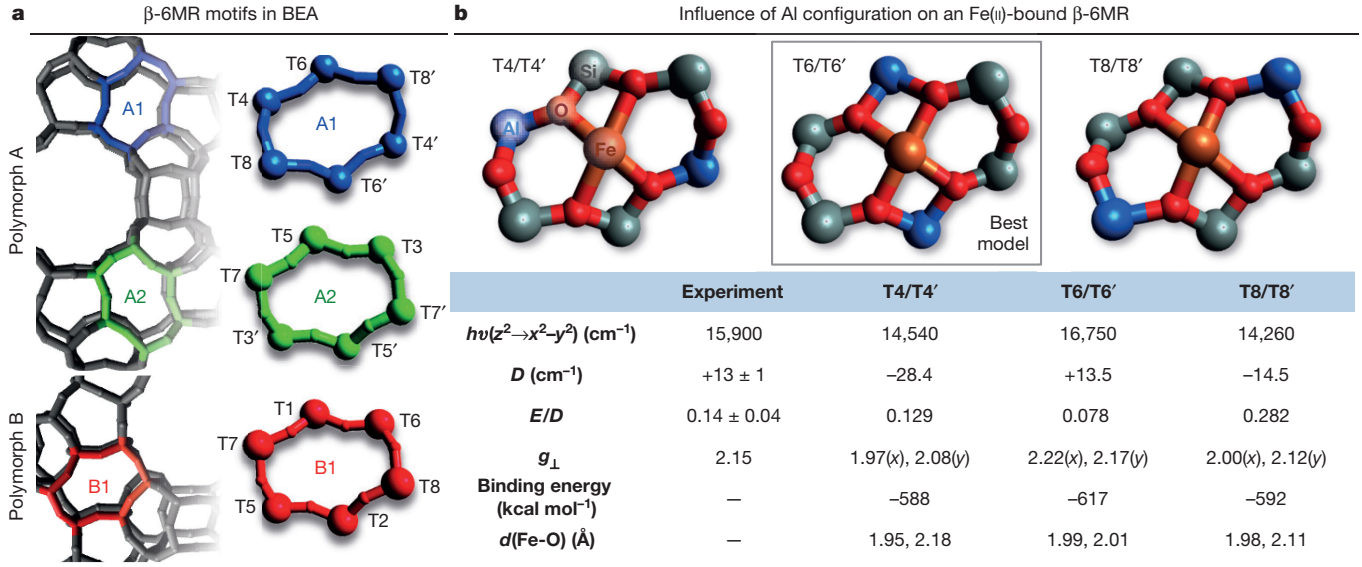

	Experiment	T4/T4′	T6/T6′	T8/T8′
$h\nu(z^2 \rightarrow x^2-y^2)$ (cm^{-1})	15,900	14,540	16,750	14,260
D (cm^{-1})	+13 ± 1	−28.4	+13.5	−14.5
E/D	0.14 ± 0.04	0.129	0.078	0.282
$g_\perp$	2.15	1.97(x), 2.08(y)	2.22(x), 2.17(y)	2.00(x), 2.12(y)
Binding energy (kcal mol^{-1})	—	−588	−617	−592
d(Fe-O) (Å)	—	1.95, 2.18	1.99, 2.01	1.98, 2.11

Figure 3 | Computational evaluation of α-Fe(II) cluster models. **a**, β-6MR motifs found in BEA polymorphs A (top) and B (bottom). **b**, Top, cluster models of ring A1 containing distinct configurations of Al tetrahedral (T)-sites (in blue; other atoms omitted for clarity); bottom, CASPT2-predicted spectral features of these Fe(II)-bound sites ($h\nu$—energy of the highest ligand field transition, D, E/D and $g_\perp$), and DFT-predicted Fe(II)-binding energies and iron-to-oxygen bond lengths (d(Fe–O)). Experimental data are provided for comparison in the first column of the table.

anionic $_{Si}O_{Al}$ ligands, while T6/T6′ binds Fe(II) with four anionic $_{Si}O_{Al}$ ligands.

We calculated spectroscopic features of the DFT-optimized cluster models at the CASPT2 level of theory (Fig. 3b and Extended Data Table 1; CASPT2 is the second-order complete active space perturbation theory). CASPT2 predicts a single, high-energy ligand-field band for all three models, thus reproducing the ligand-field spectrum of α-Fe(II) that we defined experimentally. The T4/T4′ and T8/T8′ models fail to reproduce the positive ZFS ground state of α-Fe(II), however (see Extended Data Fig. 6 and Methods). But T6/T6′ accurately reproduces both the spin Hamiltonian parameters and the ligand-field spectrum of α-Fe(II). We therefore assign α-Fe(II) as a high-spin, square planar Fe(II) site bound to a β-6MR by four anionic $_{Si}O_{Al}$ ligands. DFT-calculated Mössbauer parameters of the cluster models further support this assignment (see Methods for detail).

α-O is generated by transferring an O atom from N_2O to α-Fe(II). Low-temperature MCD data from N_2O-activated Fe(II)-BEA are shown in Fig. 4a, along with DR-UV-vis data for comparison. At least five features are observed: three relatively sharp negative bands between 5,000 cm^{-1} and 8,000 cm^{-1}, and a prominent positive band at 20,100 cm^{-1} with a low-energy shoulder. These features are not present before N_2O activation and decay upon reaction with CH_4 (see Fig. 2a and Extended Data Fig. 7), and are therefore new spectroscopic handles of α-O. We collected VTVH-MCD data from the 20,100 cm^{-1} feature (Fig. 4a, bottom). Field dependence is observed in the low-temperature saturation limit of the VTVH-MCD isofields, indicating that α-O—like α-Fe(II)—has an integer-spin ground state. Fitting a non-Kramers-doublet model to VTVH-MCD data yields a g_{eff} of 8.0 and a δ of 7 cm^{-1}. A g_{eff} of 8.0 for the ground state of α-O is consistent with either a mononuclear $S=2$ site or with a weakly coupled dimer of $S=2$ sites with oppositely signed ZFS values. The latter is excluded by Mössbauer data, which show a single quadrupole doublet for α-O ($IS=0.30$ mm s^{-1}; $|QS|=0.50$ mm s^{-1}; Extended Data Fig. 3). α-O is therefore mononuclear, and a large δ of 7 cm^{-1} indicates a positive ZFS ($+D$) ground state[11,18]. Fitting a positive ZFS $S=2$ model to VTVH-MCD data (see Methods) results in estimates of $D=8\pm1$ cm^{-1} and $E=0.5\pm0.5$ cm^{-1} for α-O.

VTVH-MCD data thus indicate that transferring an O atom to α-Fe(II) yields a mononuclear $S=2$ $[FeO]^{2+}$ site. Two electronic structures are possible: Fe(III)–$O^{\bullet-}$ or Fe(IV)=O. A D substantially larger than 2 cm^{-1} argues against an Fe(III)–$O^{\bullet-}$ ground state[18,25]. On the other hand the sign and magnitude of D for α-O are similar to known $S=2$ Fe(IV)=O sites[26,27]. Spin Hamiltonian parameters coupled with electronic structure calculations (*vide infra*) therefore define α-O to be a mononuclear $S=2$ Fe(IV)=O species.

To define factors contributing to the reactivity of α-O, we added an O atom to the cluster model of α-Fe(II). This results in a square pyramidal Fe(IV)=O species with a short, 1.59-Å Fe–O bond (Fig. 4b, top). The weak ligand field provided by the BEA lattice stabilizes the $S=2$ model (α-^{5}Fe(IV)=O), reproducing the electronic structure and Mössbauer parameters of α-O defined experimentally (see above and Methods). Computational evaluation of the reaction of α-O with CH_4 shows that H-atom abstraction (HAA) occurs on the quintet surface with a low activation barrier of 3.6 kcal mol^{-1} (Fig. 4b, middle)—consistent with the room-temperature CH_4 reactivity observed in ref. 1, and paralleling the computational results of ref. 28.

The CH_4 HAA reaction is slightly exothermic, indicating that the O–H bond strength of the Fe(III)–OH first product and the C–H bond strength of CH_4 are similar. This markedly reduces the barrier for HAA. The exceptional strength of the product O–H bond is related to the axial square pyramidal geometry of α-O, which is unstable in the absence of the zeolite lattice (see Extended Data Fig. 8 and Methods)[29,30]. Lattice constraints destabilize the ^{5}Fe(IV)=O site by about 6 kcal mol^{-1}, increasing the driving force for O–H bond formation. Adding a *trans* axial ligand mitigates this effect. Spin pairing also weakens the O–H bond (by about 12 kcal mol^{-1}; the difference between the reaction enthalpies on the quintet versus triplet surfaces; see Fig. 4b).

Given that the enthalpies of the reactant C–H bond and the product O–H bond are similar, a small $\Delta H^{\ddagger}$ (enthalpy of activation) indicates that α-O has high intrinsic reactivity towards HAA. At the transition-state geometry (when the Fe–O bond elongates from 1.59 Å to 1.72 Å), the Fe(IV)=O unit gains notable radical character, corresponding to a highly reactive Fe(III)–$O^{\bullet-}$ species. This contribution to reactivity also derives from the vacant *trans* axial position, which stabilizes the Fe($3d_{z^2}$) orbital, resulting in a highly covalent Fe=O unit. Thus, the high Fe/O covalency and the exchange stabilization of the Fe($3d$) manifold lead to an Fe(IV)=O bond that strongly spin-polarizes towards Fe(III)–$O^{\bullet-}$ at the transition-state geometry.

This direct experimental insight into the active site of low-temperature methane hydroxylation in Fe-zeolites establishes VTVH-MCD as a

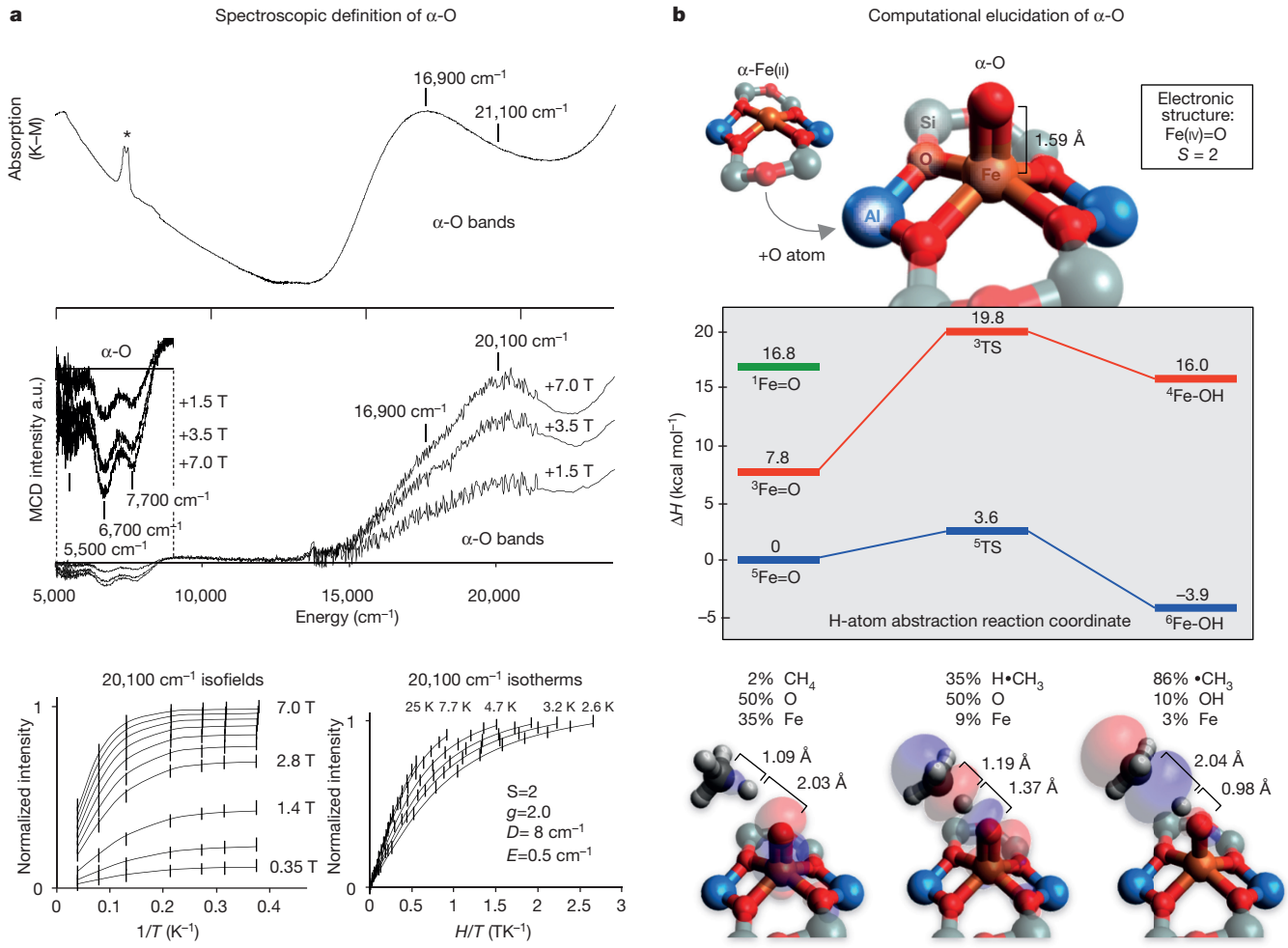

Figure 4 | Spectroscopic and computational elucidation of α-O. a, Top, room-temperature DR-UV-vis data (* = OH overtone), and middle, 3 K MCD data from N_2O-activated BEA. Bottom, VTVH-MCD saturation magnetization data from the 20,100 cm^{-1} band of α-O, including ± 1σ error bars and fit (black curves) to a positive ZFS $S = 2$ model (see Fig. 2e, right), with parameters given in inset. **b**, Top, DFT-optimized structure of α-^{5}Fe(IV)=O in the $S = 2$ ground state. Middle, energetics of the CH_4 HAA reaction. Bottom, evolution of the lowest unoccupied molecular orbital along the reaction coordinate (reactant, left; transition state, middle; and product, right).

powerful, site-selective probe of metal active sites and reactive intermediates in heterogeneous systems, delivering the level of spectroscopic insight into heterogeneous catalysis that has long been available in bioinorganic chemistry. By defining the geometric and electronic structures of α-Fe(II) and α-O and determining how these correlate to reactivity, we have been able to show that the vacant *trans* axial position of α-O, which is enforced by constraints from the zeolite lattice, is a key determinant of the intermediate's exceptional reactivity with CH_4. Thus, by preventing geometric distortion, the zeolite lattice activates α-O for reaction with CH_4, cleaving the strongest aliphatic C–H bond at room temperature to form methanol. In biology, an analogous state in which rigid constraints are used to tune enzyme metal sites for function is known as the 'entatic' state[6], and it will be important to explore further how this can be used to tune the reactivity of metal sites in heterogeneous systems.

Online Content Methods, along with any additional Extended Data display items and Source Data, are available in the online version of the paper; references unique to these sections appear only in the online paper.

Received 24 March; accepted 13 June 2016.

1. Dubkov, K. A. *et al.* Kinetic isotope effects and mechanism of biomimetic oxidation of methane and benzene on FeZSM-5 zeolite. *J. Mol. Catal. A.* **123,** 155–161 (1997).
2. Dubkov, K. A., Sobolev, V. I. & Panov, G. I. Low-temperature oxidation of methane to methanol on FeZSM-5 zeolite. *Kinet. Catal.* **39,** 72–79 (1998).
3. Ovanesyan, N. S., Shteinman, A. A., Dubkov, K. A., Sobolev, V. I. & Panov, G. I. The state of iron in the Fe-ZSM-5–N_2O system for selective oxidation of methane to methanol from data of Mössbauer spectroscopy. *Kinet. Catal.* **39,** 792–797 (1998).
4. Panov, G. I. Advances in oxidation catalysis, oxidation of benzene to phenol by nitrous oxide. *CATTech* **4,** 18–31 (2000).
5. Smeets, P. J., Woertink, J. S., Sels, B. F., Solomon, E. I. & Schoonheydt, R. A. Transition-metal ions in zeolites: coordination and activation of oxygen. *Inorg. Chem.* **49,** 3573–3583 (2010).
6. Vallee, B. L. & Williams, R. Metalloenzymes: the entatic nature of their active sites. *Proc. Natl Acad. Sci. USA* **59,** 498–505 (1968).
7. Zecchina, A., Rivallan, M., Berlier, G., Lamberti, C. & Ricchiardi, G. Structure and nuclearity of active sites in Fe-zeolites: comparison with iron sites in enzymes and homogeneous catalysts. *Phys. Chem. Chem. Phys.* **9,** 3483–3499 (2007).
8. Centi, G., Genovese, C., Giordano, G., Katovic, A. & Perathoner, S. Performance of Fe-BEA catalysts for the selective hydroxylation of benzene with N_2O. *Catal. Today* **91–92,** 17–26 (2004).
9. Jíša, K. *et al.* Role of the Fe-zeolite structure and iron state in the N_2O decomposition: Comparison of Fe-FER, Fe-BEA, and Fe-MFI catalysts. *J. Catal.* **262,** 27–34 (2009).
10. Baerlocher, C., McCusker, L. B. & Olson, D. H. *Atlas of Zeolite Framework Types* (Elsevier, Amsterdam, 2007).
11. Solomon, E. I., Pavel, E. G., Loeb, K. E. & Campochiaro, C. Magnetic circular dichroism spectroscopy as a probe of the geometric and electronic structure of non-heme ferrous enzymes. *Coord. Chem. Rev.* **144,** 369–460 (1995).
12. Burns, R. G., Clark, M. G. & Stone, A. J. Vibronic polarization in the electronic spectra of gillespite, a mineral containing iron (II) in square-planar coordination. *Inorg. Chem.* **5,** 1268–1272 (1966).
13. Cantalupo, S. A., Fiedler, S. R., Shores, M. P., Rheingold, A. L. & Doerrer, L. H. High-spin square-planar Co(II) and Fe(II) complexes and reasons for their electronic structure. *Angew. Chem. Int. Edn* **51,** 1000–1005 (2012).

14. Pinkert, D. *et al.* A dinuclear molecular iron (II) silicate with two high-spin square-planar FeO_4 units. *Angew. Chem. Int. Edn* **52,** 5155–5158 (2013).
15. Pascualini, M. E. *et al.* A high-spin square-planar Fe (II) complex stabilized by a trianionic pincer-type ligand and conclusive evidence for retention of geometry and spin state in solution. *Chem. Sci.* **6,** 608–612 (2015).
16. Xia, H. *et al.* Direct spectroscopic observation of Fe (III)-phenolate complex formed from the reaction of benzene with peroxide species on Fe/ZSM-5 at room temperature. *J. Phys. Chem. C* **112,** 9001–9005 (2008).
17. Dubkov, K. A., Ovanesyan, N. S., Shteinman, A. A., Starokon, E. V. & Panov, G. I. Evolution of iron states and formation of α-sites upon activation of FeZSM-5 zeolites. *J. Catal.* **207,** 341–352 (2002).
18. Solomon, E. I. *et al.* Geometric and electronic structure/function correlations in non-heme iron enzymes. *Chem. Rev.* **100,** 235–350 (2000).
19. Campochiaro, C., Pavel, E. G. & Solomon, E. I. Saturation magnetization magnetic circular dichroism spectroscopy of systems with positive zero-field splittings: application to $FeSiF_6{\bullet}6H_2O$. *Inorg. Chem.* **34,** 4669–4675 (1995).
20. Clark, M. G., Bancroft, G. M. & Stone, A. J. Mössbauer spectrum of Fe^{2+} in a square-planar environment. *J. Chem. Phys.* **47,** 4250–4261 (1967).
21. Wurzenberger, X., Piotrowski, H. & Klüfers, P. A stable molecular entity derived from rare iron (II) minerals: the square-planar high-spin-d6 $FeIIO_4$ chromophore. *Angew. Chem. Int. Edn* **50,** 4974–4978 (2011).
22. Newsam, J. M., Treacy, M. M. J., Koetsier, W. T. & de Gruyter, C. B. Structural characterization of zeolite beta. *Proc. R. Soc. Lond. A* **420,** 375–405 (1988).
23. Dědeček, J., Sobalík, Z. & Wichterlová, B. Siting and distribution of framework aluminium atoms in silicon-rich zeolites and impact on catalysis. *Catal. Rev. Sci. Eng.* **54,** 135–223 (2012).
24. Lowenstein, W. The distribution of aluminum in the tetrahedra of silicates and aluminates. *Am. Mineral.* **39,** 92–96 (1954).
25. Kahn, O. *Molecular Magnetism* (VCH, New York, 1993).
26. Puri, M. & Que, L. Toward the synthesis of more reactive S=2 non-heme oxoiron (IV) complexes. *Acc. Chem. Res.* **48,** 2443–2452 (2015).
27. McDonald, A. R. & Que, L. High-valent nonheme iron-oxo complexes: synthesis, structure, and spectroscopy. *Coord. Chem. Rev.* **257,** 414–428 (2013).
28. Rosa, A., Ricciardi, G. & Baerends, E. J. Is $[FeO]^{2+}$ the active center also in iron containing zeolites? A density functional theory study of methane hydroxylation catalysis by Fe-ZSM-5 zeolite. *Inorg. Chem.* **49,** 3866–3880 (2010).
29. Rossi, A. R. & Hoffman, R. Transition metal pentacoordination. *Inorg. Chem.* **14,** 365–374 (1975).
30. Neidig, M. L. *et al.* Spectroscopic and electronic structure studies of aromatic electrophilic attack and hydrogen-atom abstraction by non-heme iron enzymes. *Proc. Natl Acad. Sci. USA* **103,** 12966–12973 (2006).
31. Weckhuysen, B. M. & Schoonheydt, R. A. Recent progress in diffuse reflectance spectroscopy of supported metal oxide catalysts. *Catalysis Today* **49,** 441–451 (1999).

Supplementary Information is available in the online version of the paper.

Acknowledgements B.E.R.S. acknowledges support from the National Science Foundation Graduate Research Fellowship Program under grant DGE-11474, and from the Munger, Pollock, Reynolds, Robinson, Smith & Yoedicke Stanford Graduate Fellowship. P.V. acknowledges Research Foundation–Flanders (FWO; grant 12L0715N) and KU Leuven for his postdoctoral fellowships and travel grants during his stay at Stanford University. S.D.H. acknowledges FWO for a PhD (aspirant) Fellowship. L.U. acknowledges FWO for a postdoctoral fellowship. Funding for this work was provided by the National Science Foundation (grant CHE-1360046 to E.I.S.), and within the framework of FWO (grants G0A2216N to B.F.S and G.0865.13 to K.P.). The computational resources and services used for the CASPT2 calculations were provided by the VSC (Flemish Supercomputer Center) and funded by the Hercules Foundation and the Flemish Government department EWI.

Author Contributions E.I.S., B.F.S., R.A.S. and K.P. designed the experiments. B.E.R.S., P.V., M.L.B. and L.H.B. performed the experiments. B.E.R.S. performed the DFT calculations with help from L.H.B. S.D.H. and L.U. performed the CASPT2 calculations. B.E.R.S., P.V. and E.I.S. analysed the data. B.E.R.S. and E.I.S. wrote the manuscript with help from P.V., S.D.H. and L.U.

Author Information Reprints and permissions information is available at www.nature.com/reprints. The authors declare no competing financial interests. Readers are welcome to comment on the online version of the paper. Correspondence and requests for materials should be addressed to E.I.S. (edward.solomon@stanford.edu), B.F.S. (bert.sels@biw.kuleuven.be) or R.A.S. (robert.schoonheydt@biw.kuleuven.be).

Reviewer Information *Nature* thanks A. Bell, E. Bill and the other anonymous reviewer(s) for their contribution to the peer review of this work.

METHODS

Preparation of Fe-zeolites. We prepared samples of Fe-zeolites (Fe-beta (BEA), Fe-ZSM-5 (having a MFI topology), Fe-ferrierite (FER) and Fe-mordenite (MOR)) from the corresponding acid zeolites by diffusion impregnation of $Fe(acac)_3$ (acac = acetylacetonate) in toluene solution (10 mM; 25 ml g^{-1} zeolite). The $Fe(acac)_3$ concentration was lowered to 2.5 mM when preparing Fe-BEA samples with a lower iron content (0.3 wt%). ^{57}Fe-enriched Fe(II) BEA was synthesized similarly using a 50% mixture of labelled and non-labelled $Fe(acac)_3$. All samples were calcined in air at 550 °C to remove organic material. This preparation method minimizes Fe heterogeneity and limits the formation of oxide/hydroxide species (relative to aqueous exchange or sublimation). The samples, each approximately 1 gram, were then subjected to high-temperature treatment at 900 °C in helium for 2 hours, followed by a reductive treatment in hydrogen at 700 °C for 1 hour. A flow rate of 50 cm^3 min^{-1} was used in both gas treatments. The Fe content of the resulting Fe(II)-BEA was determined by inductively coupled plasma mass spectrometry. All subsequent manipulations were carried out under an inert atmosphere (either nitrogen or helium). N_2O activation of Fe(II)-BEA (1 gram) was performed at 250 °C using a 5 vol% N_2O/helium flow (50 cm^3 min^{-1}). From Mössbauer (Extended Data Fig. 3), a typical sample of N_2O-activated Fe-BEA (0.3 wt% Fe, Si/Al = 12) contains 42 μmol α-O per gram of catalyst (78% of total Fe content). The CH_4 reaction was performed at room temperature using a 10 vol% CH_4/helium flow (50 cm^3 min^{-1}). We recovered 30–35 μmol methanol per gram of catalyst through liquid extraction, corresponding to a 70–80% methanol yield (some methanol remains adsorbed on the zeolite).

Diffuse reflectance spectroscopy. DR-UV-vis spectra were recorded on a Varian Cary 5000 UV–VIS–NIR spectrophotometer at room temperature against a halon white reflectance standard in the range 4,000–50,000 cm^{-1}. All treatments before *in situ* UV-vis-NIR spectroscopic measurements were performed in a quartz U-tube/flow cell. The latter was equipped with a window for *in situ* UV-vis-NIR diffuse reflectance spectroscopy. After UV-vis measurement, the catalyst pellets were mounted in the quartz side arm of the U-tube, ensuring that the conditions for UV-vis-NIR and MCD/Mössbauer measurements were identical.

MCD and VTVH-MCD spectroscopy. All cells for MCD spectroscopy were prepared under an inert nitrogen atmosphere. Mull samples with suitable transparency were prepared using dried and degassed perfluoro-2-methylpentane as the mulling agent. This inert glassing agent can be rigorously dried and degassed, preserving the oxidation state and coordination environment of Fe sites in Fe-BEA. Further, its refractive index is a suitable match to Al/SiO_2 materials, minimizing signal attenuation from scattering. Mulls were frozen using liquid nitrogen immediately after preparation, with special care taken to avoid exposure to oyxgen. MCD data were collected using a Jasco J730 spectropolarimeter with a liquid nitrogen cooled InSb detector coupled to an Oxford Instruments SM4000-7T superconducting magnet. MCD spectra were background corrected for baseline effects using data collected at 0 T. VTVH-MCD data were collected using a calibrated Cernox temperature sensor (Lakeshore Cryotronics, calibrated to 1.5–300 K with 0.001 K tolerance) inserted directly into the sample cell. Isotherms/isofields were normalized to the maximum observed intensity. Spin Hamiltonian parameters were extracted from VTVH-MCD isotherms using established procedures (see below)[11,18,19,32].

VTVH-MCD analysis. As shown in Fig. 2c, rhombic ZFS mixes the $\pm M_s$ levels of a non-Kramers doublet into equal admixtures designated $|X\rangle$ and $|Y\rangle$, split by δ. $|X\rangle$ and $|Y\rangle$ are both MCD silent owing to the cancellation of oppositely signed $\pm M_s$ contributions to MCD intensity. Magnetic field parallel to the principal axis of the ZFS tensor induces MCD activity in a non-Kramers doublet by mixing $|X\rangle$ and $|Y\rangle$ through an off-diagonal Zeeman matrix element. The resulting states are eigenfunctions of the spin Hamiltonian matrix for an isolated non-Kramers doublet:

$$\hat{H} = \begin{array}{c} \\ |X\rangle \\ |Y\rangle \end{array} \begin{array}{c} \begin{array}{cc} |X\rangle & |Y\rangle \end{array} \\ \begin{bmatrix} +\delta/2 & g_{\mathrm{eff}}\beta H\cos\theta \\ g_{\mathrm{eff}}\beta H\cos\theta & -\delta/2 \end{bmatrix} \end{array}$$

In the case that $g_{\mathrm{eff}}\beta H$ (where β is the Bohr magneton and H is the magnetic field) is large relative to δ, pure $\pm M_s$ states are recovered, and the $1/T$ saturation limit attains a maximum. The sensitivity of the saturation limit to field in Fig. 2b therefore reflects the magnitude of δ. As shown in Fig. 2e, the information content of δ and g_{eff} for mononuclear high spin Fe(II) depends on the sign of the axial ZFS parameter D. For negative ZFS systems, δ is the rhombic splitting of the $M_s = \pm 2$ doublet, which should be <6 cm^{-1}. The $\delta = 9$ cm^{-1} of α-Fe(II) is well outside this range. For positive ZFS systems, the $M_s = 0$ ground state and one component of the $M_s = \pm 1$ excited state together behave as an effective $M_s = \pm 2$ non-Kramers doublet, with the magnetic field oriented perpendicular to the principal axis of the ZFS tensor. For a positive ZFS ground state, δ is this splitting, which can be large. A δ of 9 cm^{-1} therefore defines α-Fe(II) to be a $+D$ system.

The axial and rhombic ZFS parameters, D and E, can be quantified from VTVH-MCD data by including higher-temperature (4.7–20 K) isotherms. At higher temperatures, the second component of the $M_s = \pm 1$ excited state not included in the non-Kramers doublet model becomes thermally populated (Fig. 2e, right). A three-level model incorporating this component provides estimates of $D = 13 \pm 1$ cm^{-1} and $E = 1.8 \pm 0.5$ cm^{-1}. A perpendicular field is required to induce MCD activity in the $M_s = 0$ ground state of a +ZFS $S = 2$ system (this level is not sensitive to the parallel field). Thus at low temperatures (where $M_s = 0$ alone is populated), the g_{eff} of a +ZFS $S = 2$ system correlates to a molecular g value ($= g_{\mathrm{eff}}/4$)[11,29].

Fitting an $S = 2$ spin Hamiltonian to VTVH-MCD data results in similar estimates of D and E/D (ref. 32). This fitting procedure involves a considerably larger parameter space (three g values, three transition moments, E, and E/D). Initially, all three g values were fixed at the spin-only value of 2.0023 while D and E/D were incremented over the range $-20 \leq D \leq +20$ and $0 \leq E/D \leq 0.3$. This provided estimates of $D = +12$–18 cm^{-1} and $E/D = 0.15$–0.25. Fixing $g_{x,y} = 2.16$ (the value of g being defined from the non-Kramers doublet fit) and $g_z = 2.0023$ resulted in improved fits, but ultimately the same estimates of D (12–18 cm^{-1}) and E/D (0.15–0.25).

Mössbauer spectroscopy. ^{57}Fe Mössbauer spectra were recorded with a See Co. W302 resonant gamma ray spectrometer in horizontal geometry with zero external field using a 1.85 GBq source (Be window, Rh matrix). Data were collected from samples enriched with 50% ^{57}Fe. All spectra were recorded at room temperature and isomer shifts are given relative to α-iron foil at room temperature. Spectra were collected with 1,024 points and summed up to 512 points before analysing, and then fit with Lorentzian doublets using the Vinda software package for Microsoft Excel.

DFT calculations. Cluster models were generated from crystallographic coordinates of BEA polymorphs A and B[22], and dangling O groups were capped with H (see Supplementary Tables 1–3 for coordinates). Spin-unrestricted DFT calculations were performed with Gaussian 09 (ref. 33). The B3LYP functional was used for all DFT calculations. The 6-311G* basis set was used for Fe, for atoms directly coordinated to Fe, and for CH_4. The 6-31G* basis set was used for all other atoms. For geometry optimizations, the six T-sites of the six-membered rings were allowed to relax, and all other atoms were frozen (O and Si atoms at their crystallographic positions). All barriers for the CH_4 reaction were zero-point corrected. Coordinates of the DFT models of α-Fe(II) and α-Fe(IV)=O are reported in the Supplementary Information, along with coordinates of the α-Fe(IV)=O/CH_4 H-atom abstraction transition state. Mössbauer isomer shifts and quadrupole splittings were calculated from the small cluster models used for CASPT2 calculations (see below). Isomer shifts were calculated with the ORCA computational package using the B3LYP functional. The CP(PPP) basis set[34] was used on Fe, with 6-311G* on coordinating O atoms and 6-31G* on all others. A calibration curve was generated by relating the DFT-calculated electron densities at the iron nucleus $|\psi_0|^2$ values to the experimental isomer shifts for a test set of 23 structurally defined Fe complexes. The IS values of the α-Fe models were then estimated from the value of $|\psi_0|^2$ calculated for each cluster model. Quadrupole splittings were calculated using the B3LYP functional, with TZVP on Fe and coordinating O atoms, and 6-31G* on all others.

CASSCF/CASPT2 calculations. To reduce computational time, smaller clusters were constructed out of the DFT-optimized geometries as follows: the six-membered ring containing Fe(II) was cut out of the larger cluster and the dangling O atoms were capped with H at 0.95 Å. *Ab initio* calculations were performed with MOLCAS-8.1 (ref. 35). In the multiconfigurational approach used, relativistic effects were treated in two steps, both based on the Douglas–Kroll Hamiltonian[36]. Scalar terms were included in the basis-set generation and used to determine spin-free wave functions and energies through the use of the complete active space self-consistent field (CASSCF) method. Electron correlation effects were considered by means of the second-order complete active space perturbation theory (CASPT2)[37]. Next, spin-orbit coupling was treated in the mean field (AMFI)[36] by means of the restricted active space state interaction (RASSI) method[38], which uses the optimized CASSCF/CASPT2 wave functions as the basis states. From the resulting spin-orbit eigenstates, we computed the gyromagnetic tensor of the ground state by means of pseudospin $S = 2$ formalism as implemented in the SINGLE_ANISO module, in order to obtain the three main anisotropy axes and the associated gyromagnetic values (g_x, g_y, and g_z)[39]. The spin-orbit interaction was computed within all quintet (5) and all triplet (45) states with the RASSI program. Extended ANO-RCC basis sets[40,41] were used with the following contractions: [7*s*6*p*5*d*3*f*2*g*1*h*] for Fe; [4*s*3*p*2*d*1*f*] for O; [4*s*3*p*1*d*] for Si and Al; and [2*s*1*p*] for H. The active space was chosen according to the standard rules for transition-metal complexes[36]: that is, five 3*d* and five 4*d* orbitals of Fe; and bonding 2*p* orbitals

of the coordinating O atoms. The standard iterative phase estimation algorithm shift of 0.25 a.u. (ref. 42) and an imaginary shift of 0.1 a.u. (ref. 43) were used for the zeroth-order Hamiltonian for second-order perturbation theory. Correlation of the core electrons 1*s*, 2*s* and 2*p* of Fe, Si and Al and 1*s* of O was not taken into account in the CASPT2 step.

Spectroscopic features of α-Fe(II). On the basis of correlation to high-spin square planar Fe(II) sites and results from CASPT2, we assign the 15,900 cm^{-1} ligand-field band of α-Fe(II) the $3d_{z^2} \rightarrow 3d_{x^2-y^2}$ transition of a square planar site. The high energy of this transition reflects the equatorial anisotropy of the α-Fe(II) ligand field, as well as the unique stability of $3d_{z^2}$ in square planar geometry brought about by 4*s* mixing in the absence of axial ligands. The small Mössbauer |QS| of 0.55 mm s^{-1} has similar origins: the combination of an equatorial ligand field with a doubly occupied $3d_{z^2}$ orbital (that is, axial distribution of *d* electron density) leads to near-cancellation of large, oppositely signed lattice and valence contributions (respectively) to QS.

The α-Fe(II) binding site. As shown in Extended Data Fig. 5, the relative population of α-Fe(II) is maximized at low Fe loading. Reducing the Fe loading from 1.0 wt% to 0.3 wt% results in a decrease in the population of spectator sites from about 50% to just 7% (see Extended Data Fig. 3). The predominance of α-Fe(II) at low Fe loadings indicates that α-Fe(II) is the most stable Fe(II) site in Fe(II)-BEA. A sufficiently low lattice Si/Al ratio (that is, a high lattice Al content) must also be attained to stabilize α-Fe(II). Thus a threshold concentration of lattice Al is required for α-Fe(II) to form. This indicates that α-Fe(II) is bound to the BEA lattice by more than one Al T-site. Certain configurations only of aluminium are possible within a β-6MR. Aluminium T-sites separated by a single silicon T-site (that is, Al-O-Si-O-Al sequences) do not exist in BEA with Si/Al ratios greater than 10 (a Si/Al ratio of more than 12 was used here)[23]. Combined with Lowenstein's rule[24], this precludes β-6MRs containing three or more aluminium T-sites. Al-(O-Si)$_2$-O-Al sequences are, however, frequently implicated in the binding of divalent cations to zeolite lattices[23]. The three Al-(O-Si)$_2$-O-Al sequences possible within a β-6MR are shown in Fig. 3b, and these are the only configurations containing multiple Al T-sites that are possible in BEA with Si/Al ratios greater than 10.

Differences in the predicted spin Hamiltonian parameters of the three models shown in Fig. 3—in particular, differences in the sign of *D*—reflect differences in the first coordination shell of Fe. In the case of T6/T6′, Fe(II) is approximately square planar with four essentially equivalent $_{Si}O_{Al}$ ligands at 1.99–2.01 Å. This is a weak axial system, which leads to a positive *D*. For T4/T4′ and T8/T8′, Fe(II) is bound by two short (1.95–1.98 Å) Fe–$_{Si}O_{Al}$ bonds and two long (2.11–2.18 Å) Fe–$_{Si}O_{Si}$ bonds. As shown in Extended Data Fig. 5, the $_{Si}O_{Al}$ ligands bind Fe(II) more strongly, and as a result, the Fe–$_{Si}O_{Al}$ vector (approximately) defines the magnetic *z* axis for these sites. T4/T4′ and T8/T8′ are therefore best described as strong axial systems (with a rhombic perturbation), leading to a negative *D*.

The three cluster models can be further differentiated on the basis of their predicted Mössbauer parameters. The T6/T6′ model reasonably reproduces the low IS and small |QS| values of α-Fe(II) (calculated IS = 0.72 mm s^{-1} and QS = −0.95 mm s^{-1}; experimental IS = 0.89 mm s^{-1} and |QS| = 0.55 mm s^{-1}). The T4/T4′ and T8/T8′ Fe(II)-bound models yield similar calculated values of IS (0.78 mm s^{-1} and 0.81 mm s^{-1}, respectively), but larger values of QS (+1.38 mm s^{-1} and +1.15 mm s^{-1}, respectively). Reasonable agreement is also achieved for the T6/T6′ model of α-O (calculated IS = 0.22 mm s^{-1} and QS = −0.24 mm s^{-1}; experimental IS = 0.30 mm s^{-1} and |QS| = 0.50 mm s^{-1}).

Contributions to the reactivity of α-O. In order to understand the origin of the strong (>100 kcal mol^{-1}) O–H bond of α-^{6}Fe(III)-OH, we evaluated a set of high-spin Fe(III)-OH and Fe(IV)=O DFT models (see Extended Data Fig. 8). The models with square pyramidal geometry with an empty coordination site *trans* to the O ligand have the strongest O–H bonds. This geometry destabilizes the ^{5}Fe(IV)=O site relative to the ^{6}Fe(III)-OH, increasing the driving force for O–H bond formation. This is clearly illustrated with site 1, which features a macrocyclic ligand similar to the β-6MR of a zeolite. Removing an H atom from 1-^{6}Fe(III)–OH results in 1-^{5}Fe(IV)=O which, like α-^{5}Fe(IV)=O, has a vacant *trans* axial position. The strength of the 1-^{6}Fe(III)-OH OH bond is calculated to be 101 kcal mol^{-1} (versus the 102 kcal mol^{-1} C–H bond strength calculated for CH_4). A second conformation of 1-^{5}Fe(IV)=O is more stable, however. Shifting the oxo from the axial position to the equatorial position results in stronger bonding[29,30]. Exchanging a destabilizing equatorial σ-antibonding interaction (occupied $\sigma^*d_{x^2-y^2}$) for a stabilizing axial σ-bonding interaction (vacant $\sigma^*d_{z^2}$) stabilizes the site by 4.5 kcal mol^{-1}. After correction for the strain in the macrocyclic ligand, this difference increases to 6.0 kcal mol^{-1}. This quantifies the 'entatic' contribution to the strength of the O–H bond in 1-^{6}Fe(III)-OH.

Site 2-^{6}Fe(III)-OH, which features a similar first coordination sphere to 1-^{6}Fe(III)-OH but without geometric constraints, has a substantially weaker O–H bond. Removing an H atom from 2-^{6}Fe(III)-OH causes the O ligand to shift from the axial to the equatorial position. Because of a lack of geometric constraints, the axial isomer is not a stable minimum for 2-^{5}Fe(IV)=O. As a result, there is no entatic contribution to the O–H bond strength for this site, and the O–H bond of 2-^{6}Fe(III)-OH is weakened by 6 kcal mol^{-1} relative to 1-^{6}Fe(III)-OH (95 kcal mol^{-1} versus 101 kcal mol^{-1}). Constraining site 2 to be square pyramidal destabilizes 2-^{5}Fe(IV)=O site by 6 kcal mol^{-1}, resulting in a similar O–H bond strength to site 1.

Site 3 is qualitatively similar to site 1, in that removing an H atom from 3-^{6}Fe(III)-OH results in the axial conformation of 3-^{5}Fe(IV)=O. The O–H bond strength of 3-^{6}Fe(III)-OH is 95 kcal mol^{-1}. Site 4 is formed by adding a *trans* axial ammonia ligand to site 3. The O–H bond of 4-^{6}Fe(III)-OH is 7 kcal mol^{-1} weaker than that of 3-^{6}Fe(III)-OH (88 kcal mol^{-1} versus 95 kcal mol^{-1}). Adding an axial ligand mitigates the ligand-field stabilization-energy-based driving force for O–H bond formation (*vide supra*). The additional ligand also stabilizes the oxidized Fe(IV) site over the reduced Fe(III) site (that is, causing a change in reduction potential), further weakening the O–H bond.

32. Neese, F. & Solomon, E. MCD C-term signs, saturation behavior, and determination of band polarizations in randomly oriented systems with spin $S \geq 1/2$. Applications to $S = 1/2$ and $S = 5/2$. *Inorg. Chem.* **38,** 1847–1865 (1999).
33. Frisch, M. J. *et al. Gaussian 09, Revision E.01* (Gaussian, Wallingford, 2009)
34. Neese, F. Prediction and interpretation of the ^{57}Fe isomer shift in Mössbauer spectra by density functional theory. *Inorg. Chim. Acta* **337,** 181–192 (2002).
35. Aquilante, F. *et al.* Molcas 8: new capabilities for multiconfigurational quantum chemical calculations across the periodic table. *J. Comp. Chem.* **37,** 506–541 (2016).
36. Andersson, K., Malmqvist, P.-Å. & Roos, B. O. Second-order perturbation theory with a complete active space self-consistent field reference function. *J. Chem. Phys.* **96,** 1218–1226 (1992).
37. Hess, B. A., Marian, C. M., Wahlgren, U. & Gropen, O. A mean-field spin-orbit method applicable to correlated wavefunctions. *Chem. Phys. Lett.* **251,** 365–371 (1996).
38. Malmqvist, P. A., Roos, B. O. & Schimmelpfennig, B. The restricted active space (ras) state interaction approach with spin–orbit coupling. *Chem. Phys. Lett.* **357,** 230–240 (2002).
39. Chibotaru, L. F. & Ungur, L. Ab initio calculation of anisotropic magnetic properties of complexes. I. Unique definition of pseudospin hamiltonians and their derivation. *J. Chem. Phys.* **137,** 064112 (2012).
40. Roos, B. O., Lindh, R., Malmqvist, P. A., Veryazov, V. & Widmark, P. O. New relativistic ANO basis sets for transition metal atoms. *J. Phys. Chem. A* **109,** 6575–6579 (2005).
41. Roos, B. O., Lindh, R., Malmqvist, P. A., Veryazov, V. & Widmark, P. O. Main group atoms and dimers studied with a new relativistic ano basis set. *J. Phys. Chem. A* **108,** 2851–2858 (2004).
42. Ghigo, B., Roos, B. O. & Malmqvist, P. A. A modified definition of the zeroth-order Hamiltonian in multiconfigurational perturbation theory (CASPT2). *Chem. Phys. Lett.* **396,** 142–149 (2004).
43. Forsberg, N. & Malmqvist, P. A. Multiconfiguration perturbation theory with imaginary level shift. *Chem. Phys. Lett.* **274,** 196–204 (1997).

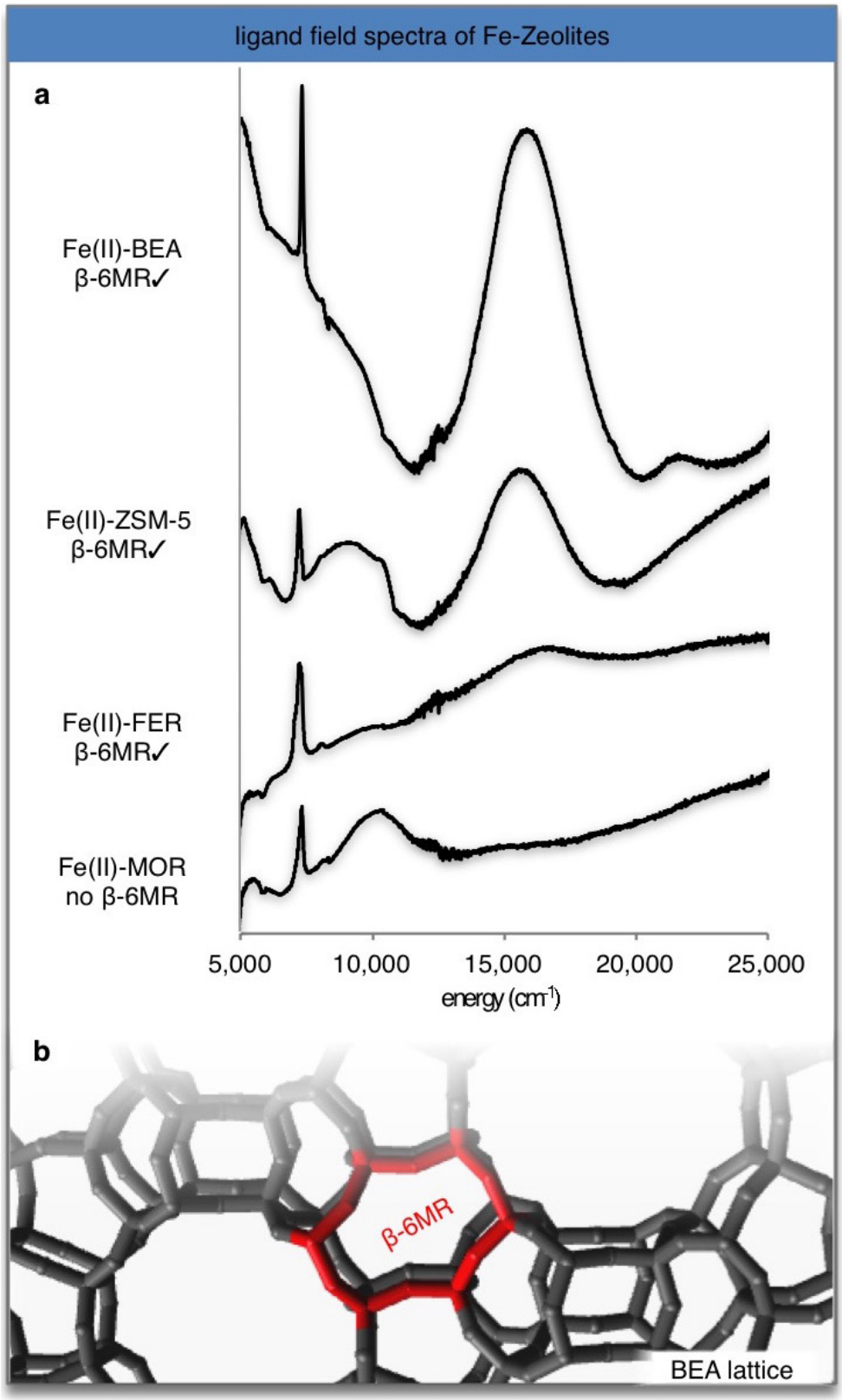

Extended Data Figure 1 | DR-UV-vis spectra of Fe-zeolites. a, Ligand-field DR-UV-vis spectra of three Fe(II)-zeolites that are known to contain α-Fe(II): Fe(II)-BEA, Fe(II)-ZSM-5, and Fe(II)-FER. Fe(II)-MOR, which does not stabilize α-Fe(II), is included for comparison. The lattice topologies that stabilize α-Fe(II) have a conserved structural motif—the β-type six-membered ring (β-6MR). **b**, An example of a β-6MR is highlighted in this BEA lattice[22].

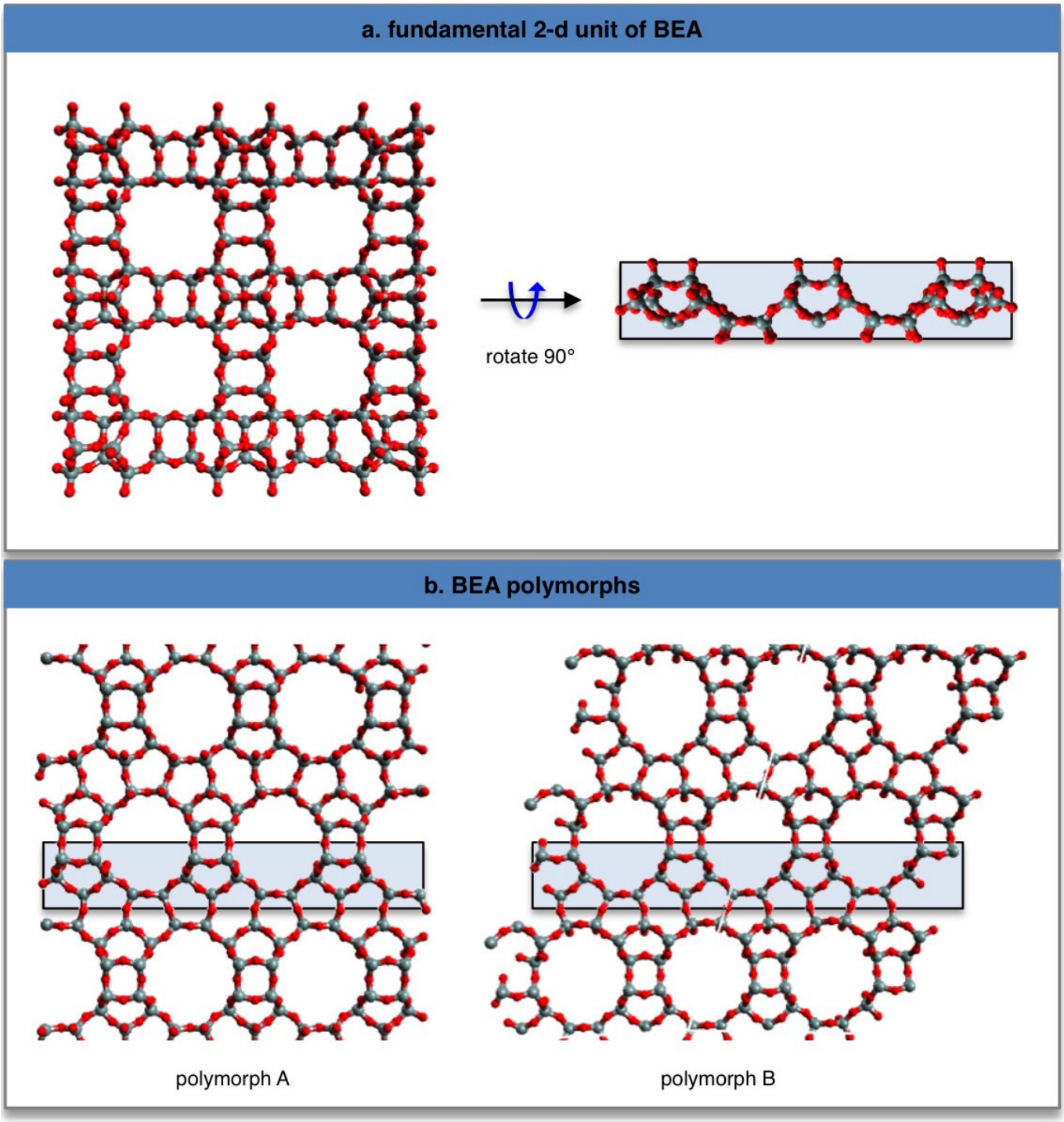

Extended Data Figure 2 | The BEA lattice. a, The structure of the fundamental two-dimensional building unit of BEA. BEA is a layered structure built up from this unit. **b**, BEA is a disordered intergrowth of two polymorphs, BEA-A and BEA-B, which result from different layerings of the same fundamental two-dimensional building unit (highlighted in blue). Both polymorphs feature three-dimensional networks of 10 Å × 10 Å channels, large enough to accommodate CH_4 and other small molecules[22].

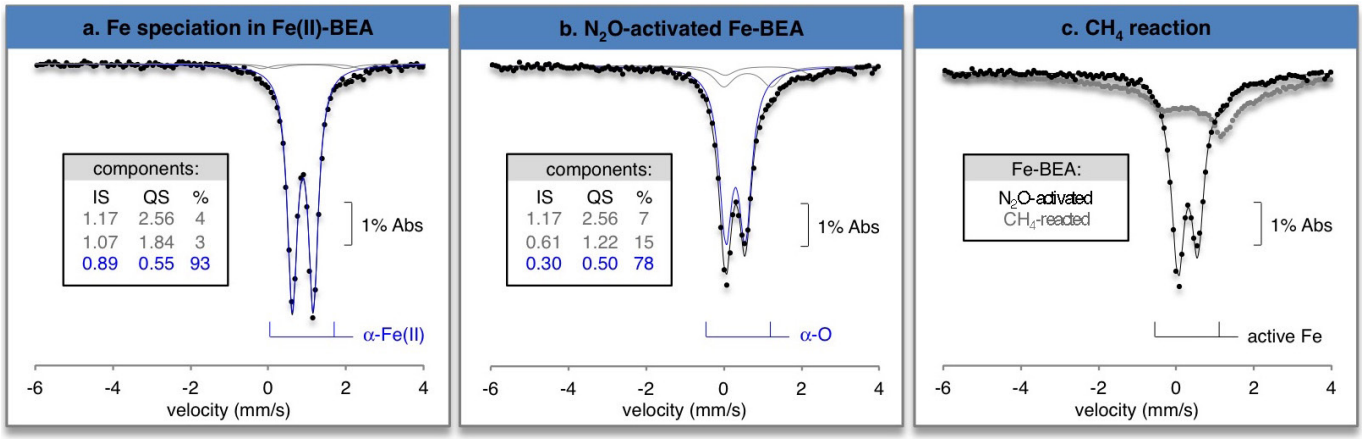

Extended Data Figure 3 | Mössbauer features of Fe-BEA. a, Room-temperature Mössbauer data were collected from a sample of Fe(II)-BEA containing 0.3 wt% Fe. Three Fe components were resolved. Abs, absorption. **b**, Reacting Fe(II)-BEA with N_2O results in loss of the IS $= 0.89\,mm\,s^{-1}$ major species and appearance of a new major component (IS $= 0.30\,mm\,s^{-1}$; 78%). **c**, This new major species is eliminated upon reaction with CH_4 at room temperature. It is therefore assigned to α-O. The IS $= 0.89\,mm\,s^{-1}$ component of Fe(II)-BEA is thus assigned to α-Fe(II). Similar Mössbauer features have also been observed in Fe-ZSM-5 and Fe-FER, but they have not been assigned to α-Fe(II)[9].

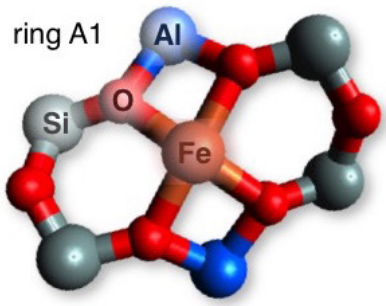

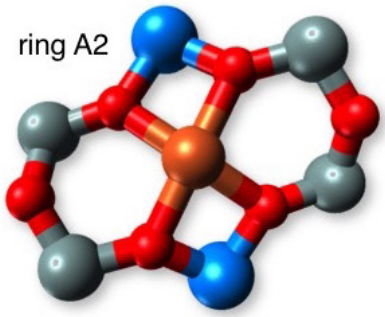

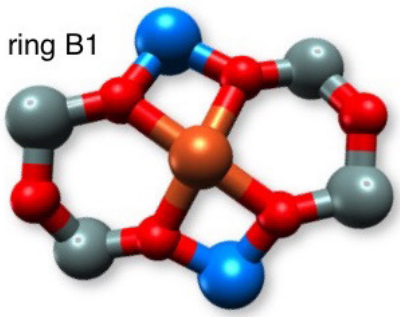

from CASPT2:	ring A1 (T6/T6')	ring A2 (T5/T5')	ring B1 (T1/T2)
$E(z^2 \rightarrow x^2\text{-}y^2)$ (cm^{-1})	16,750	16,890	16,550
D (cm^{-1})	+13.5	+13.7	+13.5
E/D	0.078	0.119	0.104
g_{perp}	2.22(x), 2.17(y)	2.24(x), 2.16(y)	2.23(x),2.16(y)
$\Delta E_{binding}$ (kcal/mol)	-617	-618	-625
d(Fe-O) (Å)	1.99, 2.01	1.99, 2.01	1.99, 2.01

Extended Data Figure 4 | Influence of β-6MR identity on predicted spectral features. DFT-calculated structures of analogous Fe(II) sites formed in each of the three types of β-6MR present in BEA (rings A1 and A2 in polymorph A, and B1 in polymorph B). Other atoms have been omitted for clarity. The table shows that the three sites are highly similar with respect to their metrical parameters, DFT-predicted Fe(II) binding energies, and CASPT2-predicted spectral features.

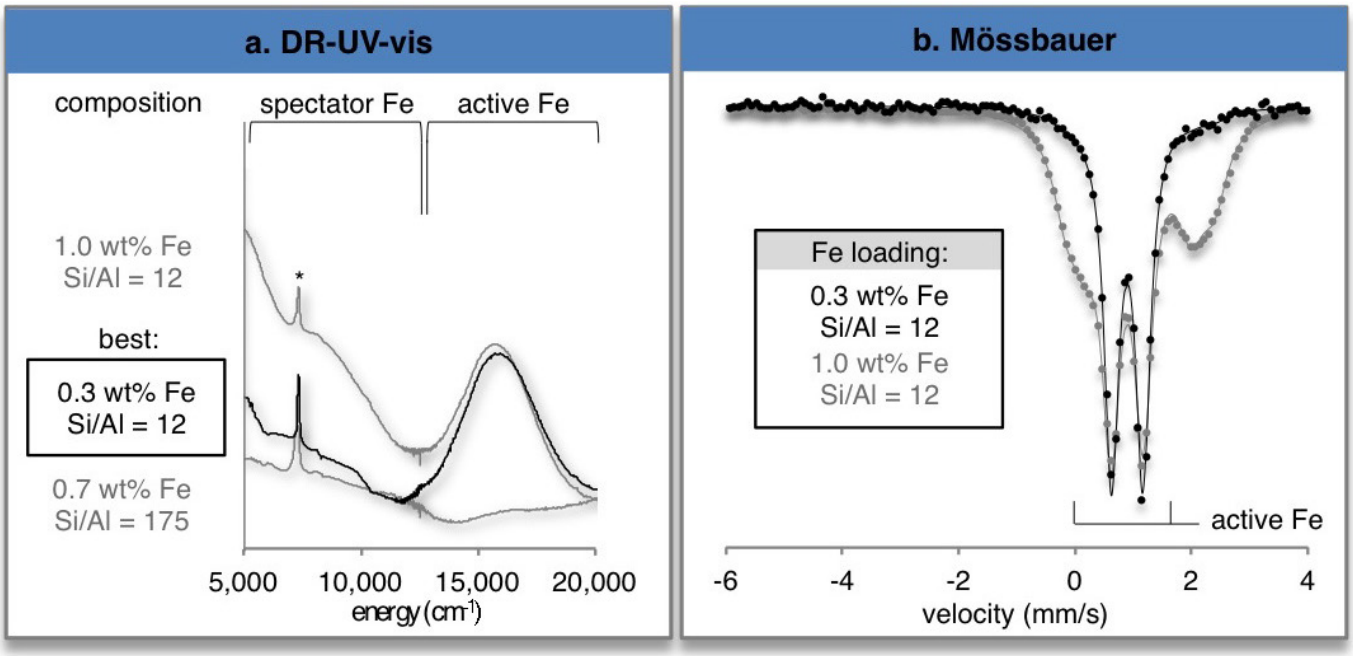

Extended Data Figure 5 | Influence of catalyst preparation on Fe speciation. a, DR-UV-vis spectra (* = OH overtone) and **b**, Mössbauer spectra of Fe(II)-BEA, showing the influence of the lattice Si/Al ratio and Fe loading on Fe speciation.

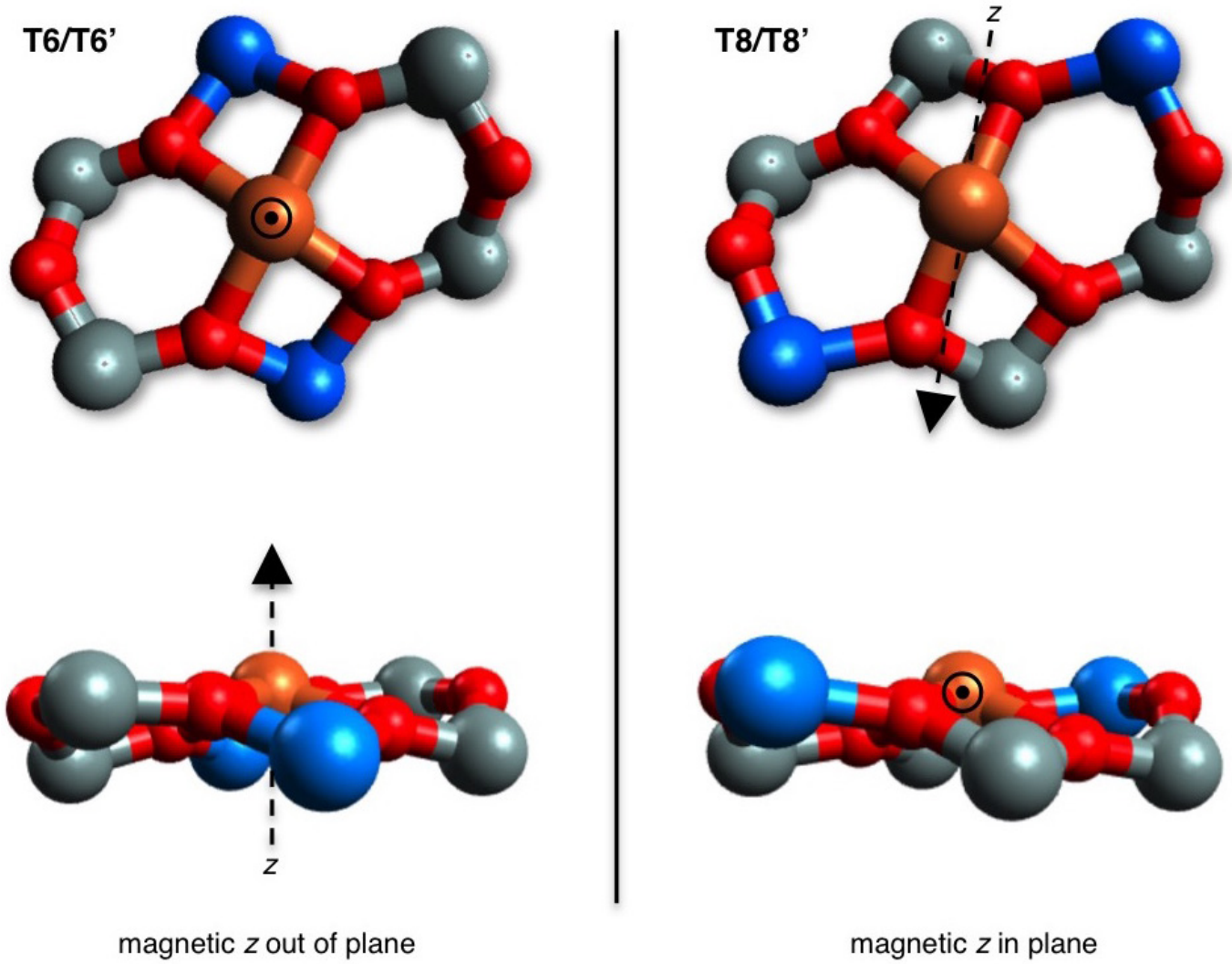

Extended Data Figure 6 | Magnetic axes of the cluster models. Orientation of the magnetic *z* axes of the T6/T6′ (left) and T8/T8′ (right) cluster models. Atoms have been omitted for clarity.

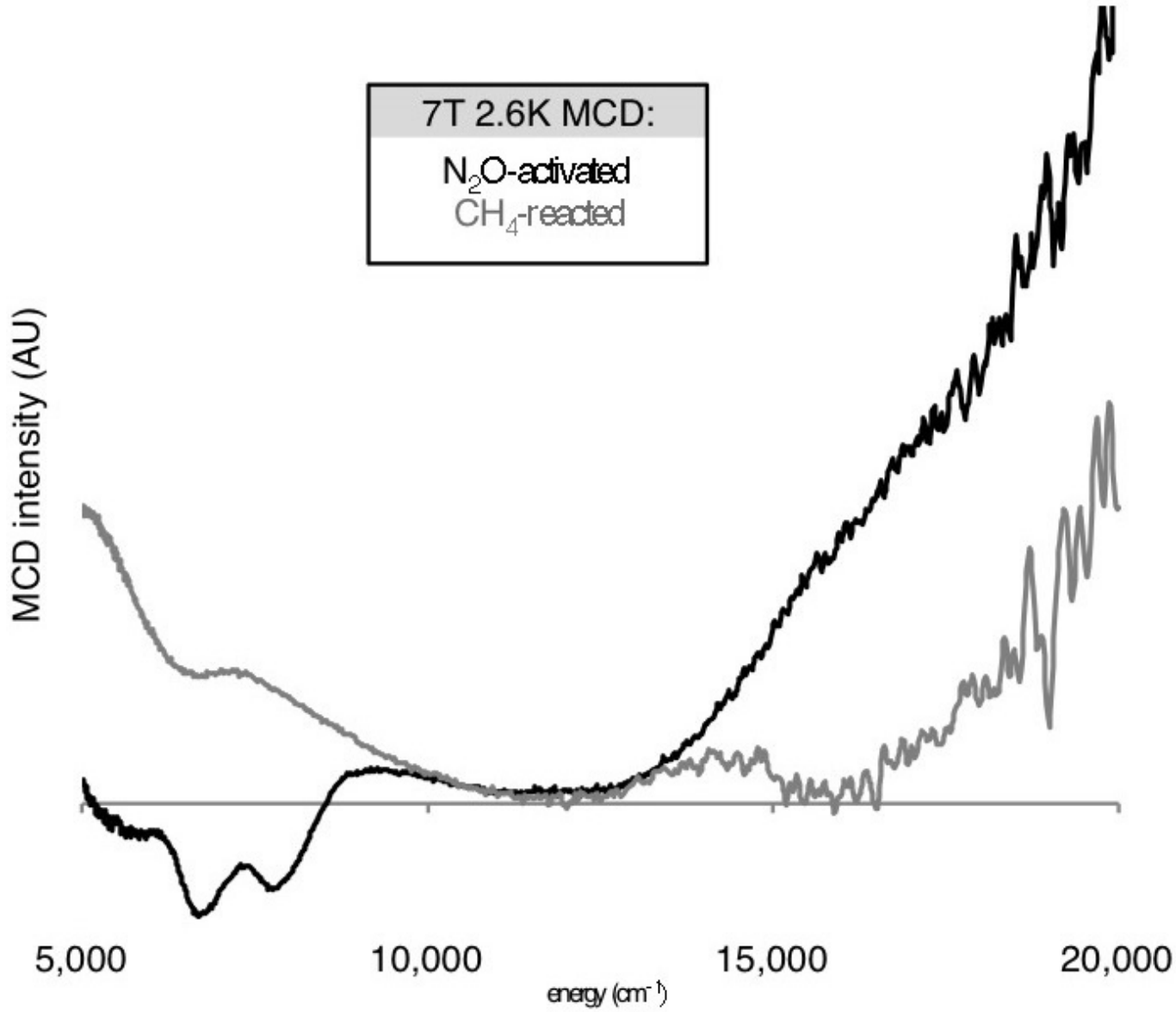

Extended Data Figure 7 | MCD features of CH_4-reacted Fe-BEA. Comparison of MCD data, collected at a temperature of 2.6 K and a field of 7 T, from N_2O-activated Fe-BEA before (black trace) and after (grey trace) reaction with CH_4 at room temperature.

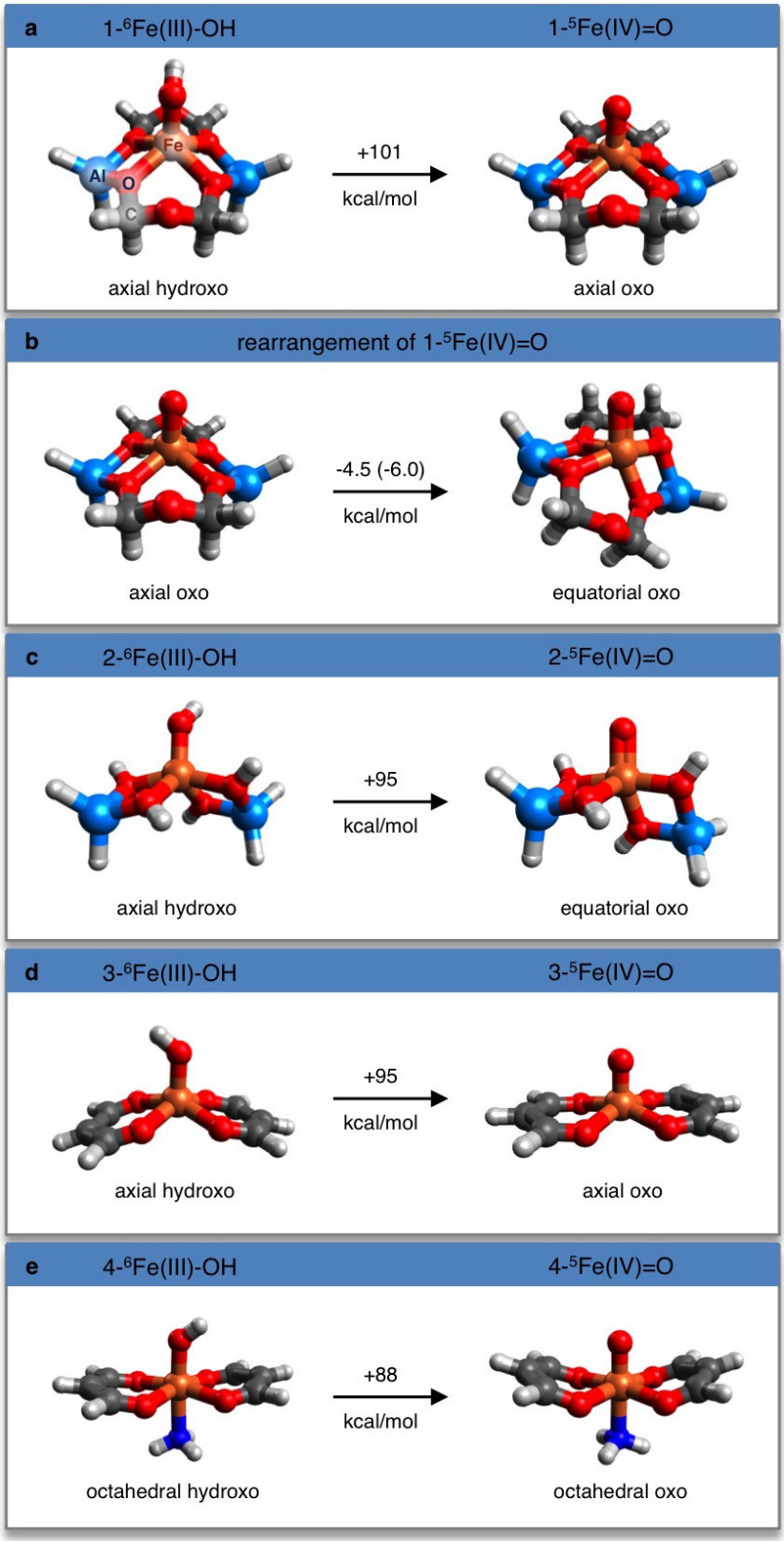

Extended Data Figure 8 | Influence of Fe(III)-OH geometry on O–H bond strength. Shown are models of $S = 5/2$ Fe(III)-OH sites and the associated $S = 2$ Fe(IV)=O species, with O–H bond strengths indicated on the arrows. **a**, Site 1 features a dianionic macrocyclic ligand resembling a β-6MR of a zeolite. **b**, Geometry optimization of the axial oxo structure in **a** shows that this site 1 conformation is destabilized by 4.5 kcal mol^{-1} (or 6.0 kcal mol^{-1}, after correcting for strain of the macrocylic ligand). **c**, Site 2 is bound by two bidentate $[AlH_2(OH)_2]^-$ ligands resembling Al T-sites. **d**, **e**, Sites 3 (**d**) and 4 (**e**) are bound by acac-like bidentate ligands (3-oxo-propenolate).

Extended Data Table 1 | Excitation energies and oscillator strengths for $S=2$ Fe(II) candidate structures

excitation	T4/T4'		T6/T6'		T8/T8'	
	energy	o.s.	energy	o.s.	energy	o.s.
$z^2 \rightarrow xz$	817	8.8×10^{-8}	2214	3.2×10^{-7}	1946	1.2×10^{-7}
$z^2 \rightarrow yz$	4158	4.8×10^{-7}	3183	2.2×10^{-8}	3361	2.7×10^{-8}
$z^2 \rightarrow xy$	3538	7.9×10^{-7}	4016	1.2×10^{-7}	3672	5.0×10^{-7}
$z^2 \rightarrow x^2-y^2$	14541	1.8×10^{-5}	16750	7.5×10^{-5}	14260	3.9×10^{-5}

The table shows the CASPT2 (refs 8, 11) excitation energies (in cm^{-1}) and corresponding oscillator strengths (o.s.) of ligand-field excited states for the different $S=2$ Fe(II) candidate structures derived from the β-6MR ring A1. In all cases the $3d_{z^2} \rightarrow 3d_{x^2-y^2}$ transition is the highest-energy ligand-field excitation (the *x*- and y-axis are defined by the Fe–$O_{lattice}$ bonds). This transition has the highest calculated oscillator strength, by one to two orders of magnitude.